Supplementary Information

Phonon-Driven Transient Bandgap Renormalization in Perovskite Single Crystals

Lijie Wang[a], Hong Wang[a,b], Razan Nughays[a], Wojciech Ogieglo[a], Jun Yin[c], Luis Gutiérrez-Arzaluz[a,b], Xinyuan Zhang[b], Jian-Xin Wang[a], Ingo Pinnau[a], Osman M. Bakr[b] & Omar F. Mohammed[a,b*]

(*omar.abdelsaboor@kaust.edu.sa*)

[a]Advanced Membranes and Porous Materials Center (AMPM), Division of Physical Science and Engineering, King Abdullah University of Science and Technology, Thuwal 23955-6900, Kingdom of Saudi Arabia.

[b]KAUST Catalysis Center, Division of Physical Sciences and Engineering, King Abdullah University of Science and Technology, Thuwal 23955-6900, Kingdom of Saudi Arabia.

[c]Department of Applied Physics, The Hong Kong Polytechnic University, Kowloon 999077 Hong Kong, P. R. China.

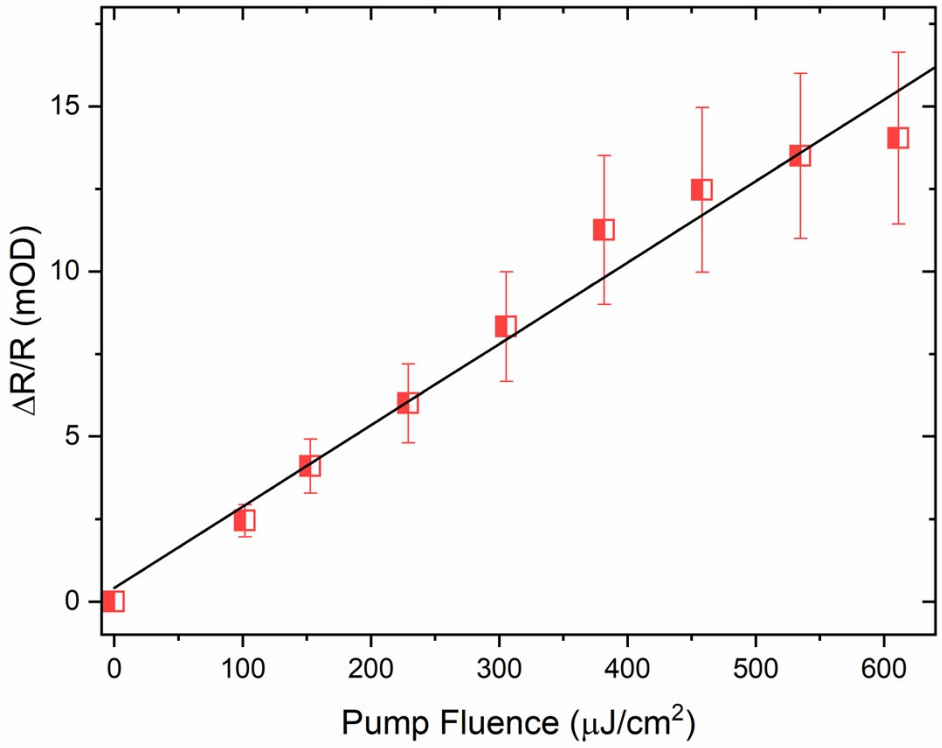

Figure S1. The pump fluence dependent transient signal intensity values (multiplied by -1) at the bleach maximum positions around 2.32 eV, the error bar was fixed to be 20% and the black line represents the linear fit in relation to pump fluences.

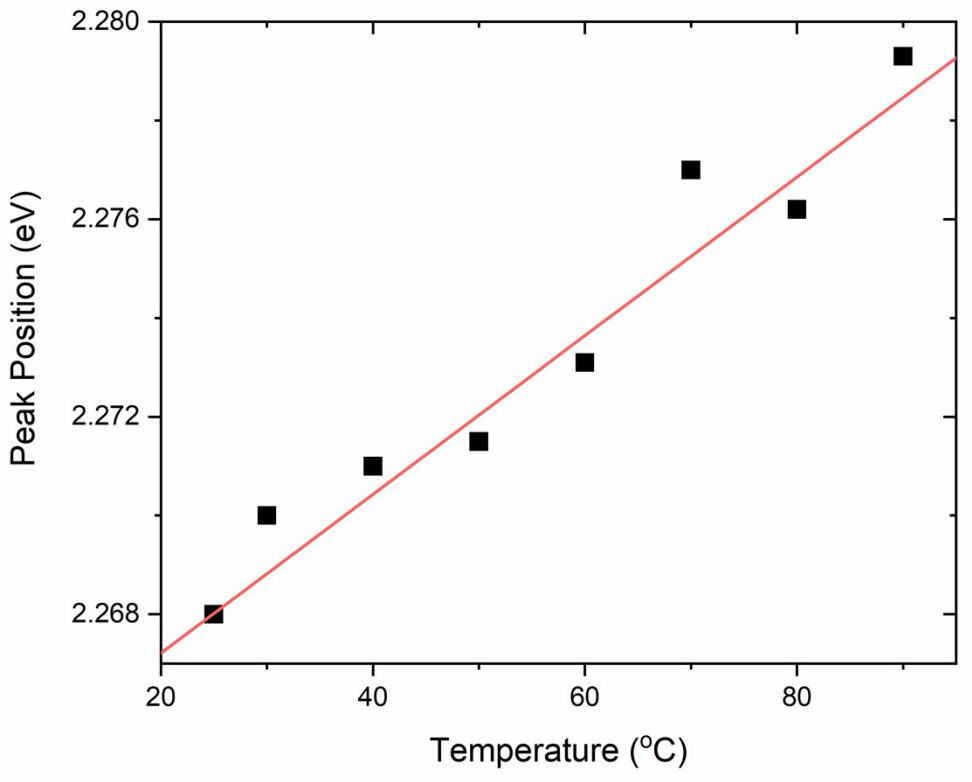

Figure S2. The peak positions of the PL shift with temperature increase, the solid red line is the linear fit.

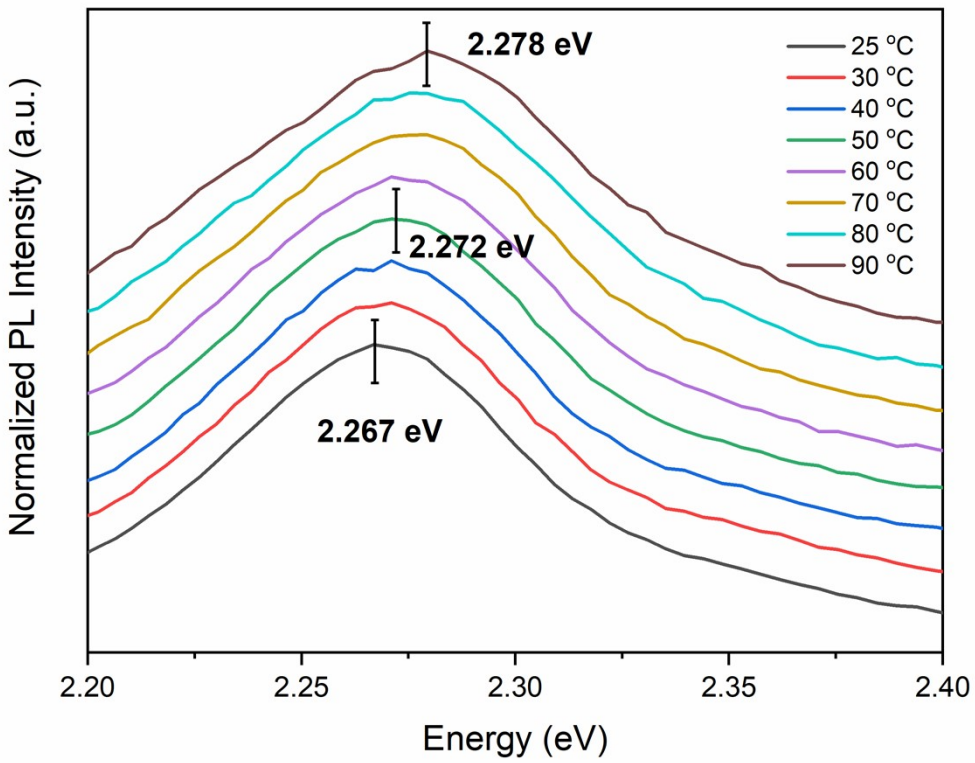

Figure S3. Normalized PL spectra, measured at different temperatures (from 25 to 90 °C), the vertical lines indicate the peak energy positions.

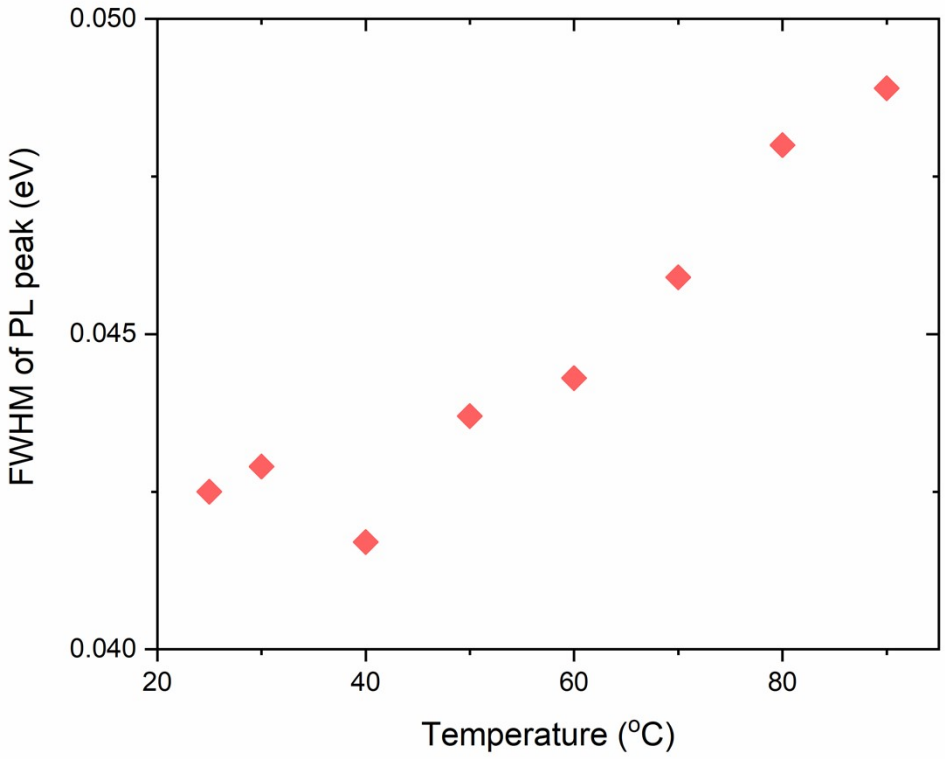

Figure S4. The FWHM of the normalized PL peak as a function of increasing the temperature.

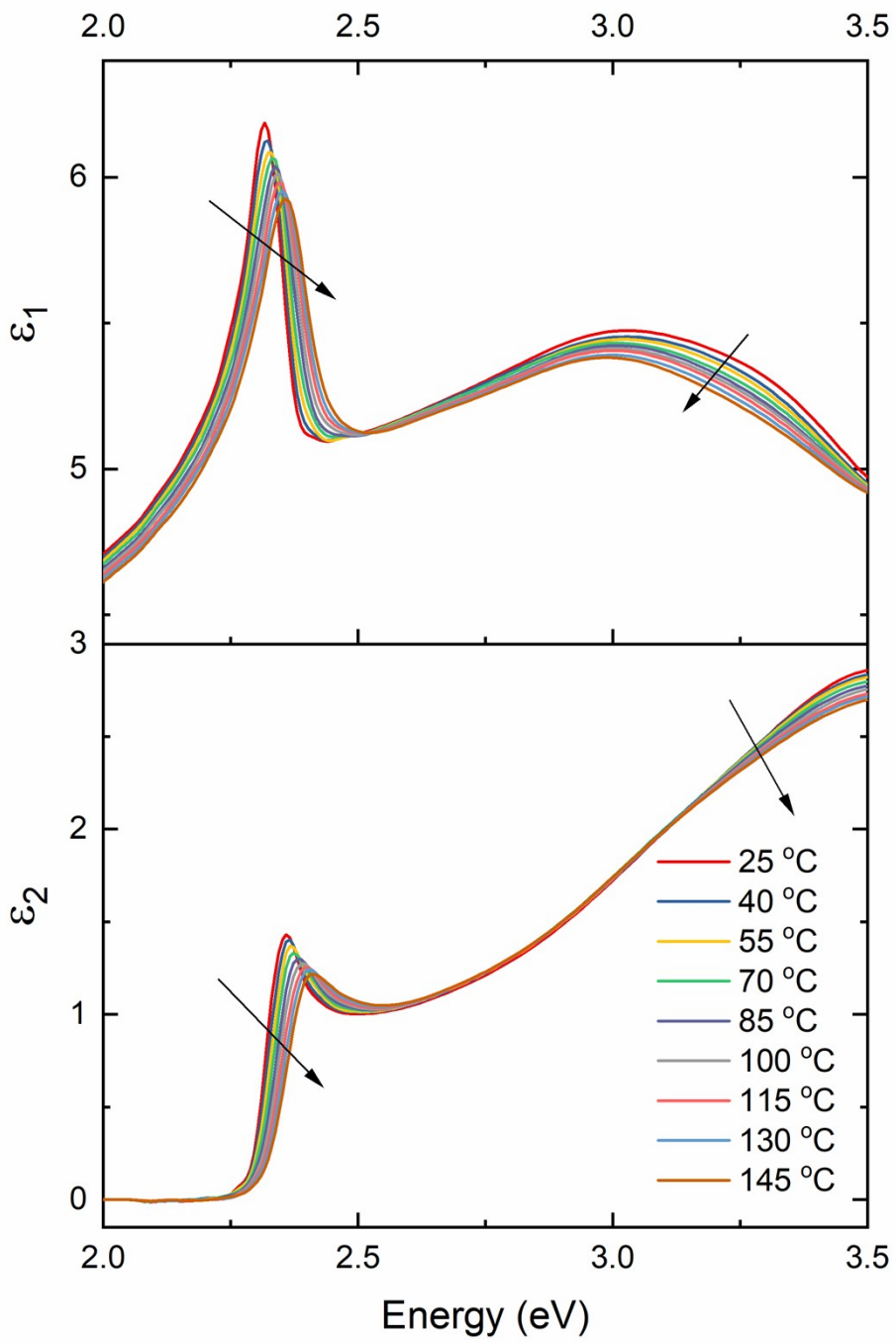

Figure S5. The temperature-dependent real (ε_1) and imaginary (ε_2) parts of the dielectric function of $MAPbBr_3$ single crystal, measured as a function of energy and temperature.

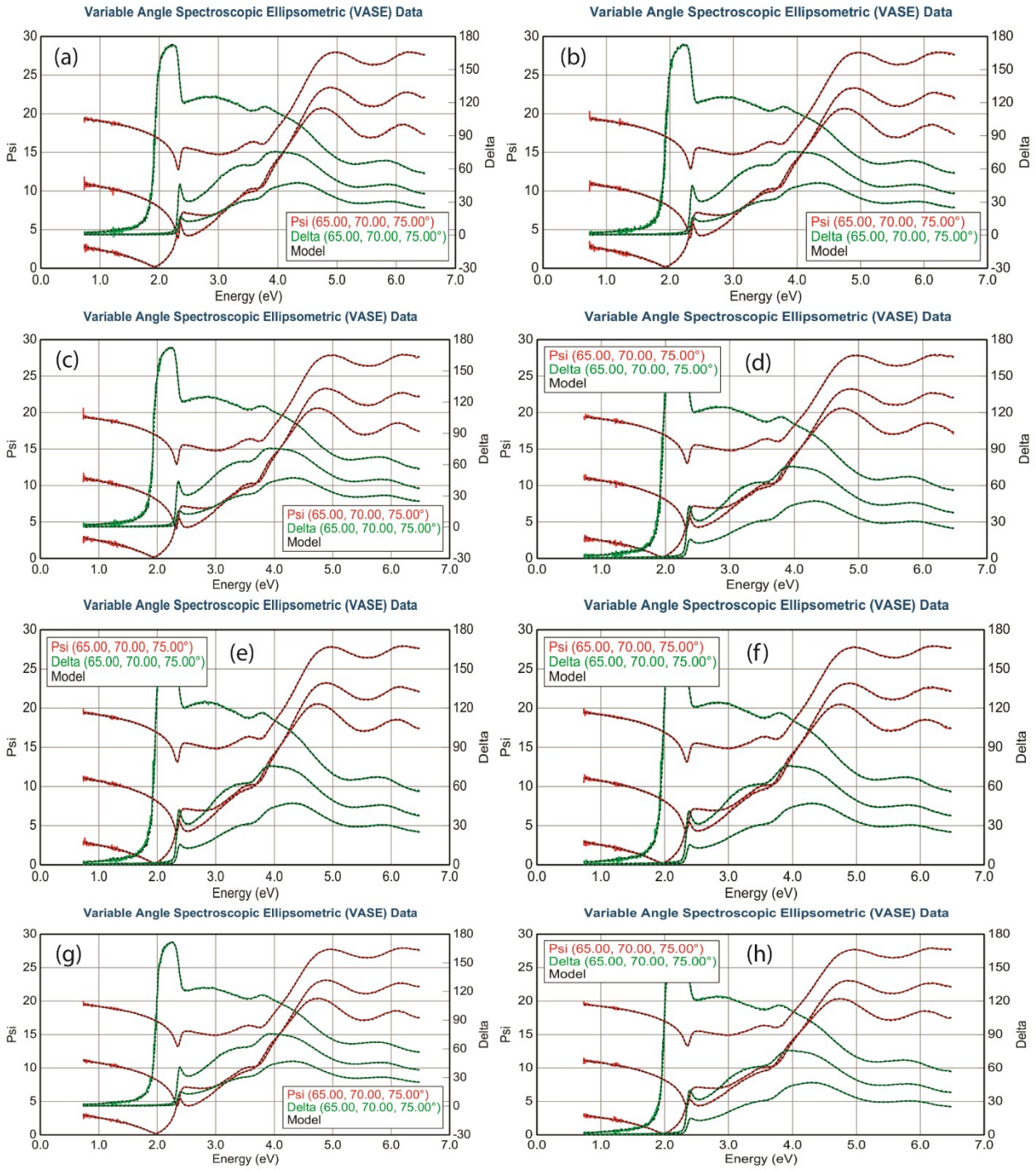

Figure S6. The variable angle spectroscopic ellipsometry data measured at 65°, 70°, and 75°, measured at different temperatures from 25 to 145 °C with 15 °C intervals (shown in Figure a-h). The dots are the experimental data, and the solid lines are the fits. The dielectric function, absorption and refractive index are extracted based on these fits.

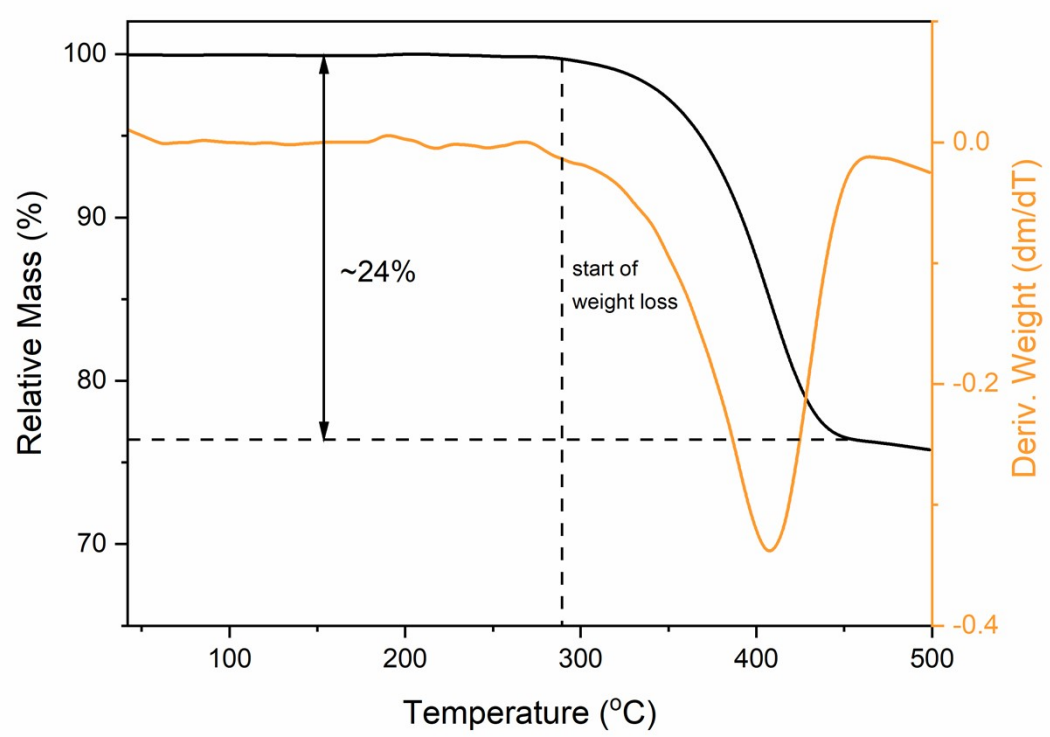

Figure S7. Thermo-gravimetric analysis (TGA) of $MAPbBr_3$ single crystal (heating rate: 20 °C/min). The loss of the relative mass and the respective derivative against temperature are shown in black and orange lines, respectively.

The melting point is far beyond the temperature range of our steady-state measurements (25-90 °C and 25-145 °C), suggesting that within our temperature range, the $MAPbBr_3$ crystals are stable.

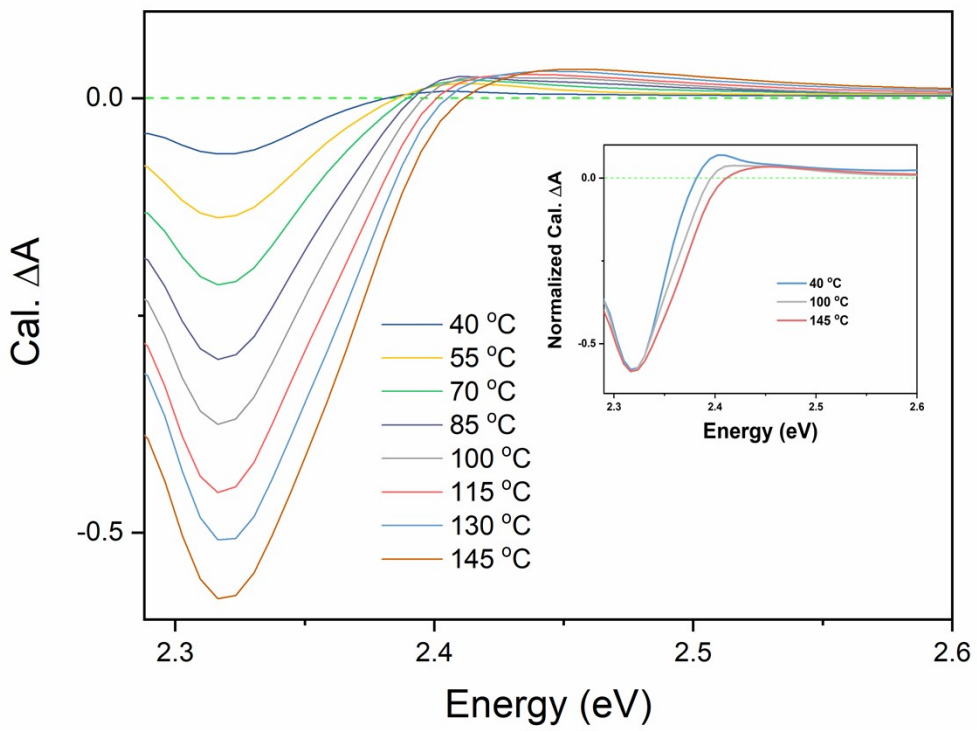

Figure S8. The simulated differential absorption, by subtracting the absorption at high temperature with that at room temperature (25 °C). The inset shows the representative normalized differential absorption spectra measured at temperature of 40, 100 and 145 °C, respectively.

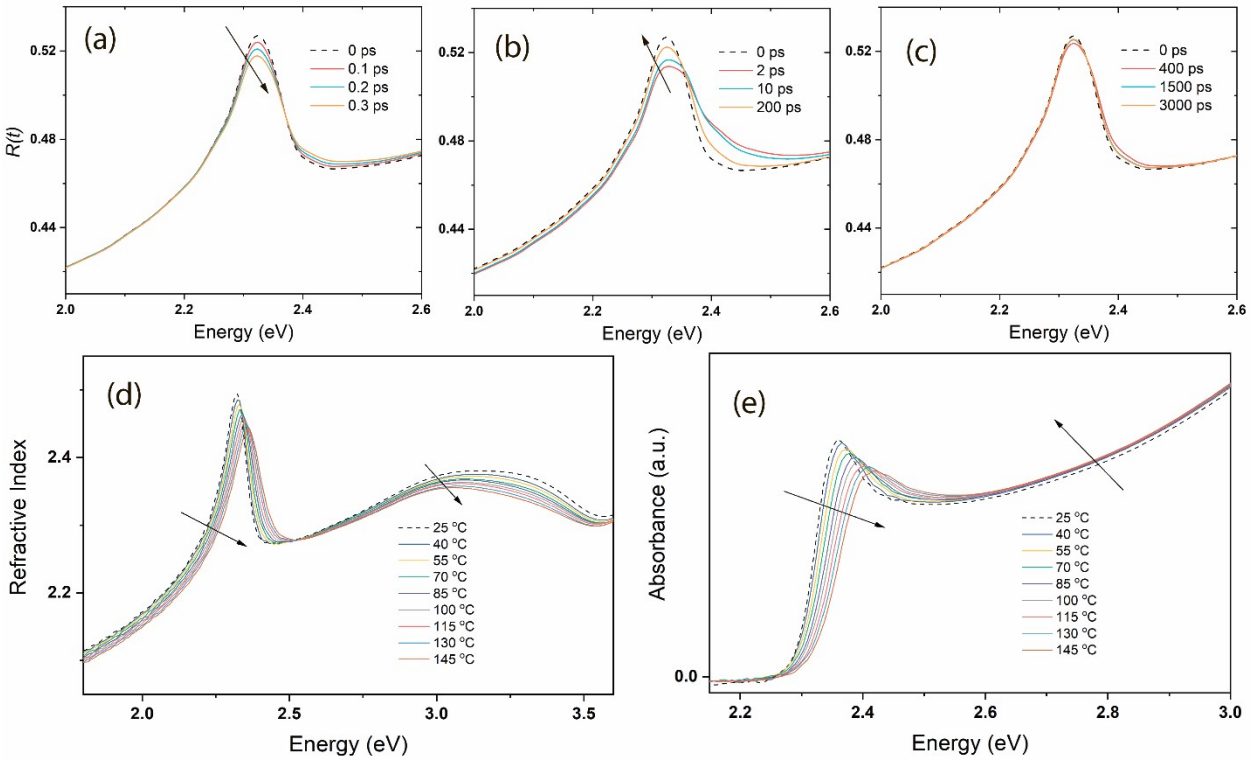

Figure S9. Spectral evolution of $R(\omega, t)$, obtained by combining the steady-state $R_s(\omega)$ calculated from ellipsometry and the $\Delta R/R(t)$ data, at (a) 0.1, 0.2, and 0.3 ps; (b) 2, 10, and 200 ps; (c) 400, 1500, and 3000 ps. (d) The extracted refractive index as a function of energy at different temperatures measured from 25 to 145 °C. (e) The absorption spectra as a function of energy at different temperatures measured from 25 to 145 °C.

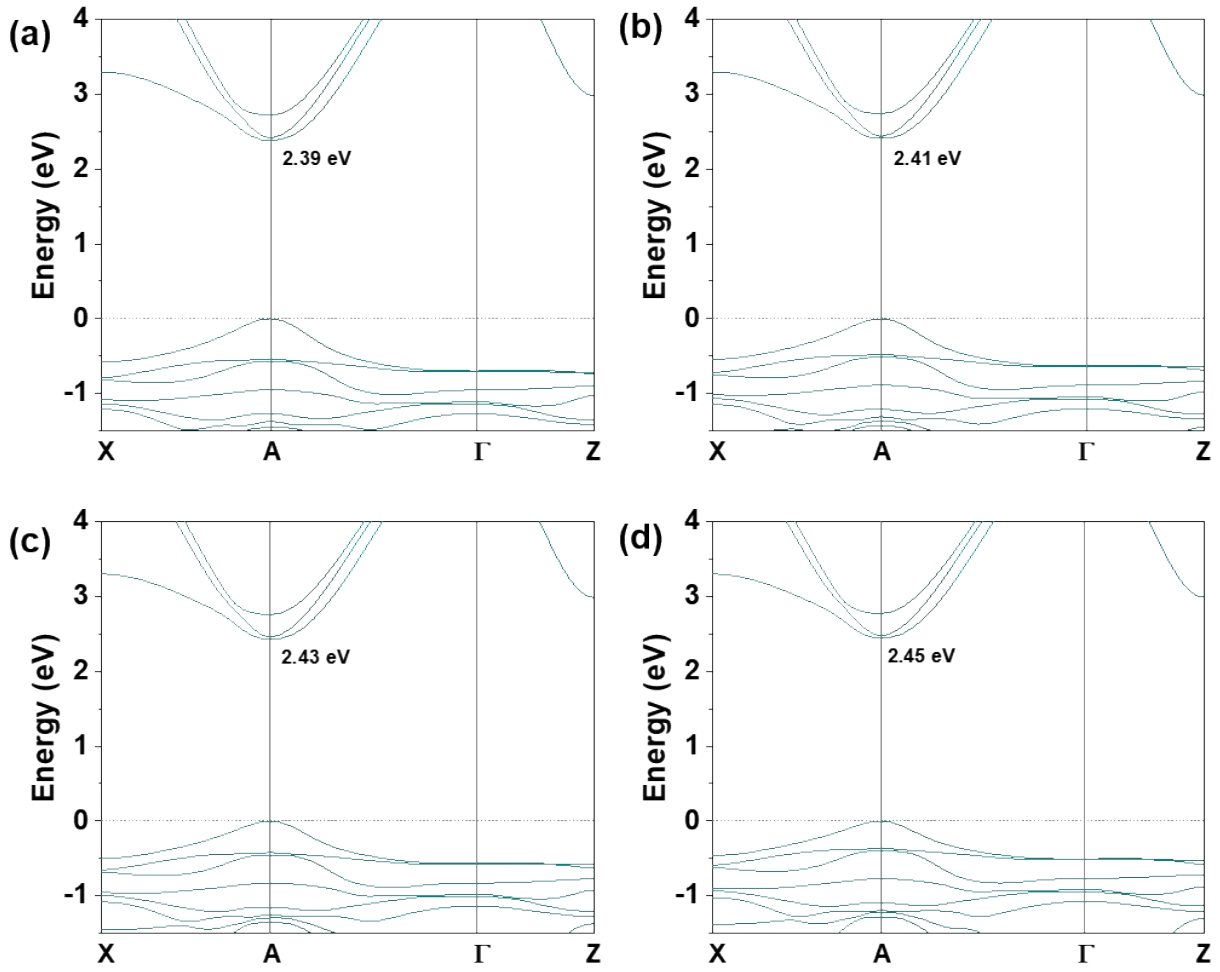

Figure S10. Electronic band structures for cubic-phase $MAPbBr_3$ with the lattice expansion of (a) 0.5%, (b) 1.0%, (c) 1.5%, and (d) 2.0%. The calculations were performed at GGA/PBE level of theory.

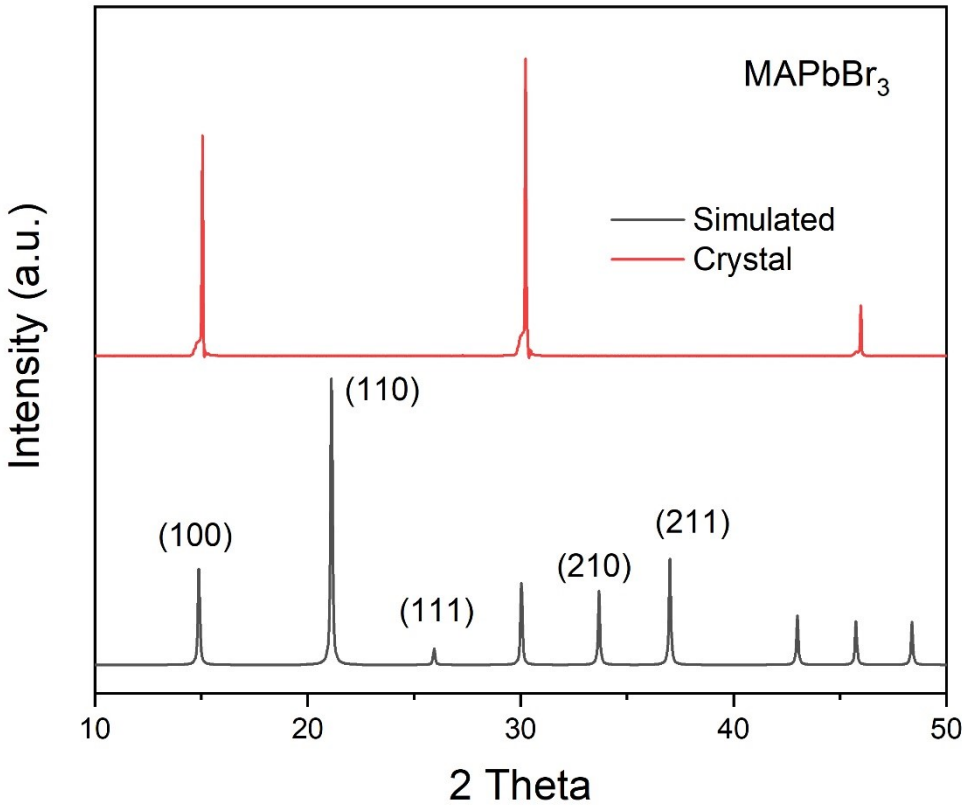

Figure S11. XRD pattern of $MAPbBr_3$ single crystal; the lower panel shows the simulated XRD from the structural data, while the upper panel shows the measured XRD from the top of the crystal.

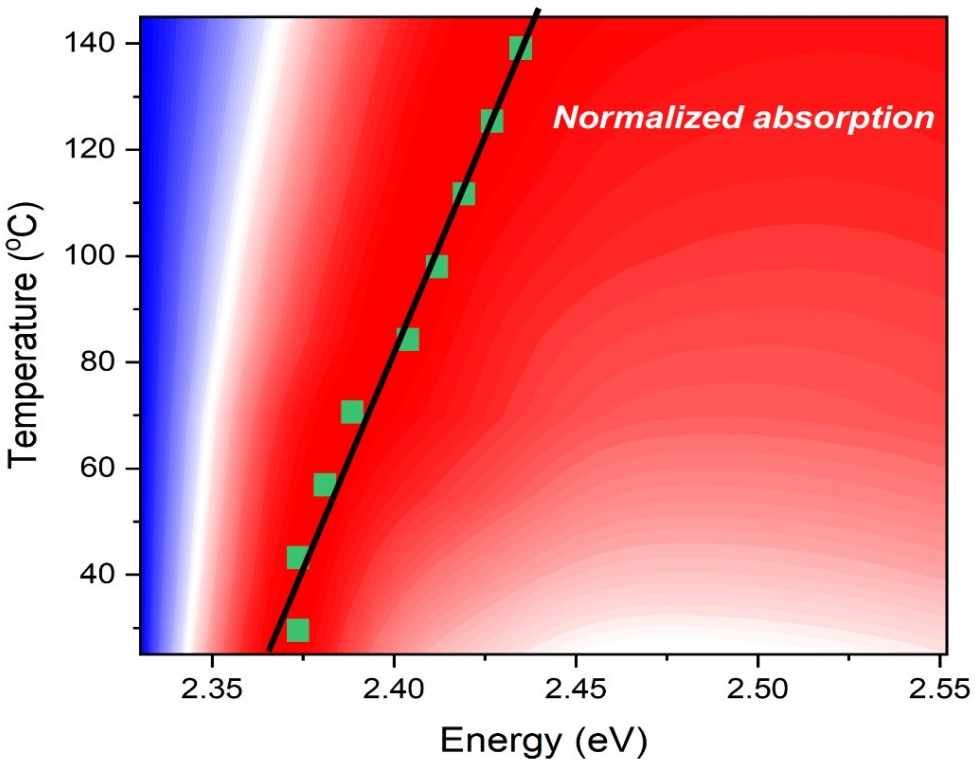

Figure S12. The normalized absorption map at the first exciton peak as function of experiment temperatures and probe energies, the green squares show the signal maxima positions of the first exciton peak at each temperature, the solid black line shows its linear fit.

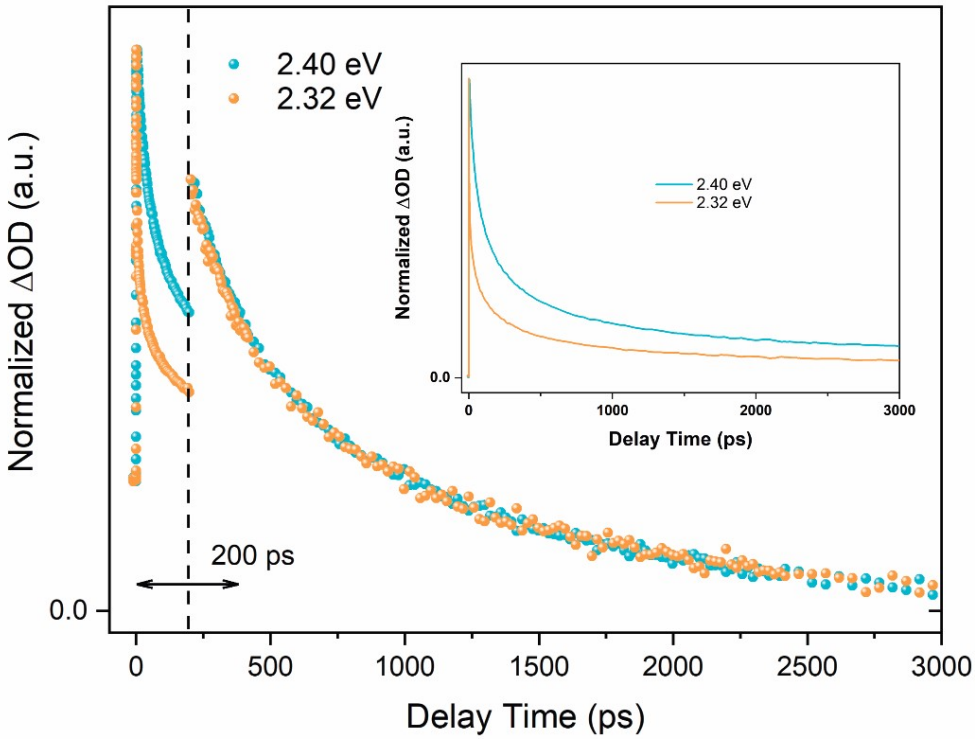

Figure S13. The transient time traces of $MAPbBr_3$ crystal probed at 2.40 and 2.32 eV, respectively. On the left side (<200 ps), the two traces are normalized at the signal maximum at ~1 ps; on the right side (<200 ps), the traces are normalized at the signal maximum at 200 ps. The inset shows the full-time traces normalized at the signal maximum at ~ 1 ps.

Figure S13 plots the kinetics at the signal maximum/minimum of the positive and negative at 2.40 and 2. 32 eV, respectively, but divided into two parts (<200 and > 200 ps) and are both normalized at the signal maximum. From the transients, the two features have an obvious asymmetric evolution; however, this kinetic deviation mainly occurs within the first 200 ps, after ~200 ps, the decays at the two bands nearly have an identical speed.

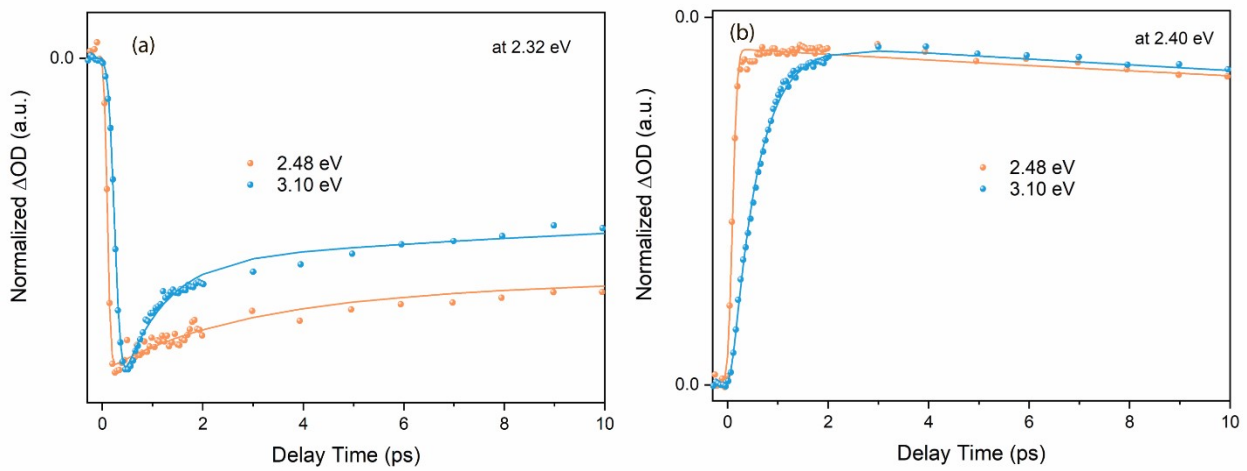

Figure S14. The short-term time traces probed at (a) 2.32 eV and (b) 2.40 eV upon 2.48 and 3.10 eV excitation, respectively. The dots represent the experimental data and the solid lines are the fits.

The kinetic behaviors of $MAPbBr_3$ crystal under different excitation energies are different at both positive and negative bands, both for rising and decaying. With higher excess energy, the rising of the transient signal is slow, which means that the generated hot electrons take a longer time to cool down to the bottom of the conduction band. In addition, with low excitation energy (2.48 eV), the bleach signal at 2.32 eV lacks a fast decay component, this was explained in terms of an absence of hot-hole cooling from valance band 2 to valance band 1[1].

Table S1. The fitting time constants of the kinetic probed at 2.32 and 2.40 eV, upon 3.10 eV excitation with 305.6 μJ/cm^2.

	τ_1 (ps)	**τ_1 (ps)**	**τ_3 (ps)**
2.40 eV	0.72±0.2	67.1±2.8	633.0±37
2.32 eV	0.59±0.1	25.1±5.0	419.5±62

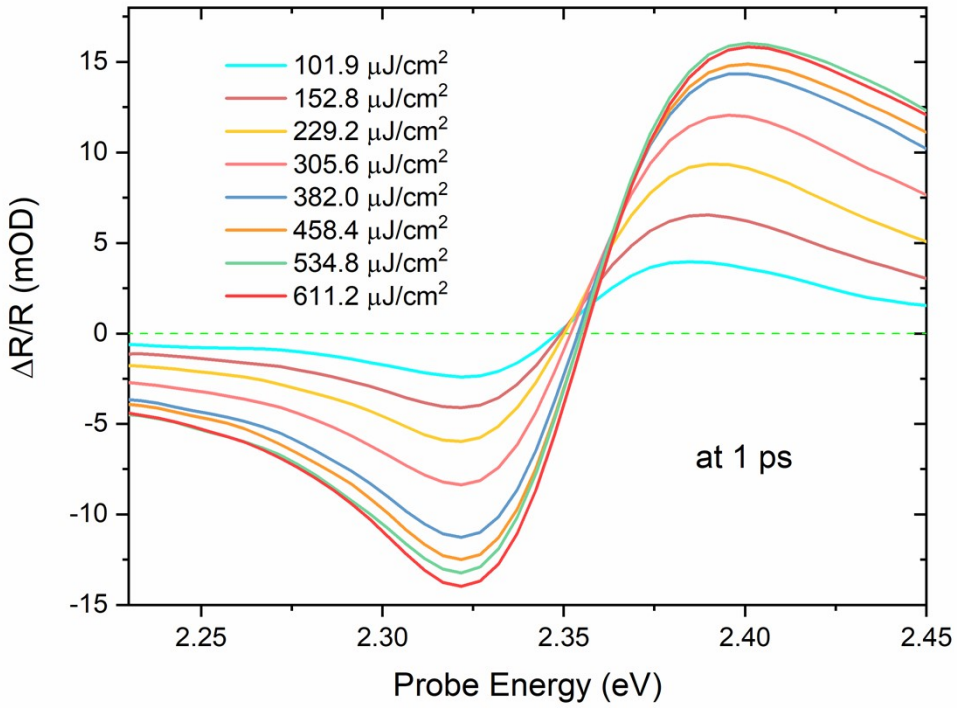

Figure S15. The pump fluence dependent transient spectral traces of $MAPbBr_3$ crystal cutting at 1 ps.

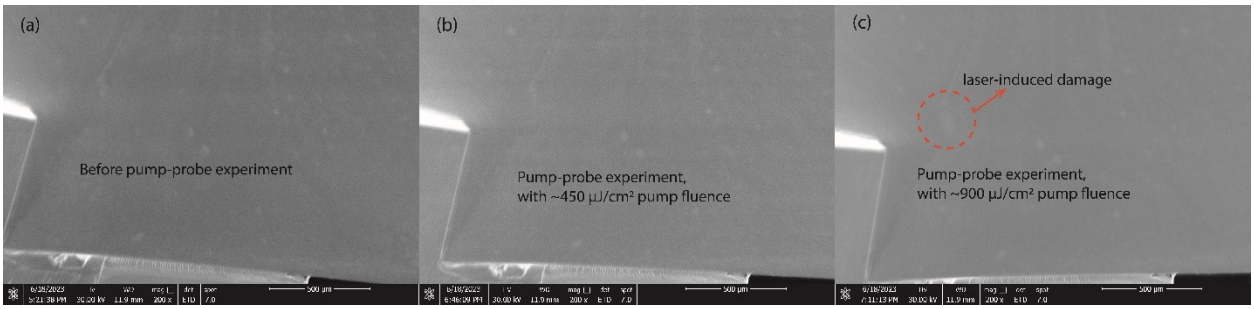

Figure S16 (a) SEM image of the $MAPbBr_3$ crystal surface at 200x magnification before conducting pump-probe experiments. (b) SEM image of the crystal surface after pump-probe experiments, demonstrating no observable damage at pump fluences up to approximately 450 μJ/cm^2. (c) SEM image of the crystal surface after pump-probe experiments, highlighting a laser-induced damage area indicated by the dashed red circle, resulting from an excitation of ~900 μJ/cm^2 at 3.1 eV.

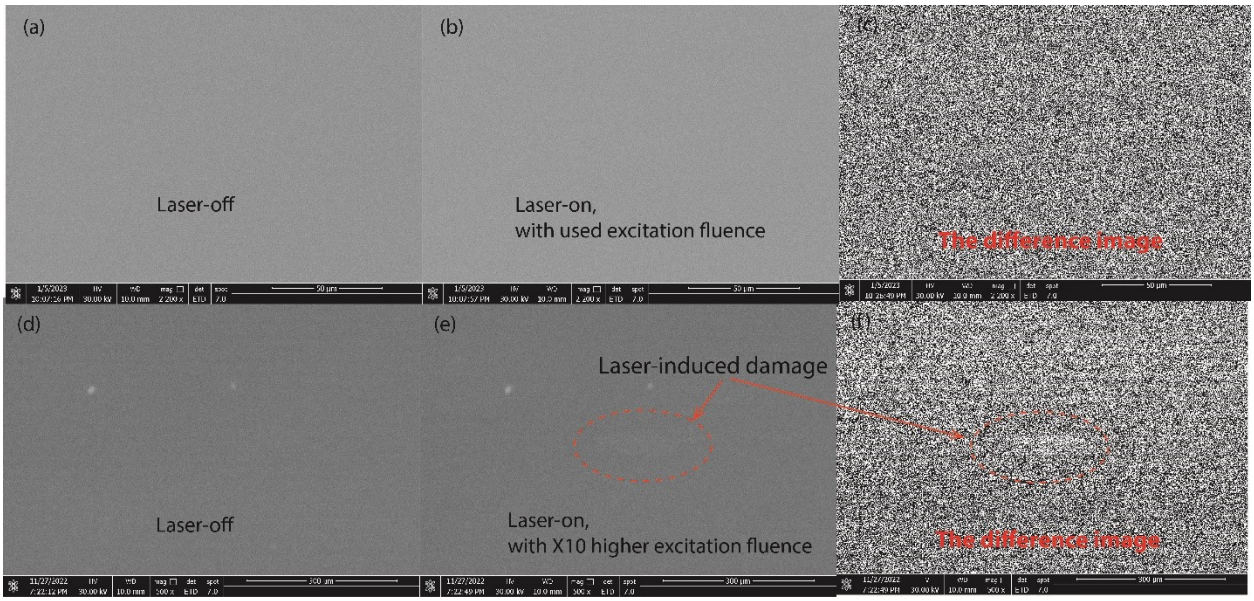

Figure S17 (a) SEM image of the $MAPbBr_3$ crystal surface without laser irradiation. (b) SEM image of the crystal surface under laser irradiation, using an identical excitation fluence as in the time-resolved SEM measurements. (c) Difference image obtained by subtracting the SEM image in figure b from figure a. (d) SEM image of the crystal surface without laser irradiation, at 500x magnification. (e) SEM image of the crystal surface under laser irradiation, using a 10-fold higher excitation fluence than that used in the time-resolved SEM measurements. A laser-induced damage spot is clearly visible at the center of the image, indicated by the dashed red circle. (f) Difference image obtained by subtracting the SEM image in figure e from figure d, showing a distinct bright spot caused by the high laser fluence, highlighted by the dashed red circle.

References

1. Xing, G. *et al.* Long-range balanced electron-and hole-transport lengths in organic-inorganic $CH_3NH_3PbI_3$. *Science* **342**, 344–347 (2013).